JOURNAL OF GEOPHYSICAL RESEARCH, VOL. 105, NO. B9, PAGES 21,579–21,590, SEPTEMBER 10, 2000

Multichannel analysis of shear wave splitting

Sébastien Chevrot
Department of Earth, Atmospheric and Planetary Sciences,
Massachusetts Institute of Technology, Cambridge

Abstract. A multichannel analysis is introduced to constrain seismic anisotropy from the shear wave splitting of SKS and $SKKS$. This technique utilizes simultaneously a set of records coming from different azimuths. The splitting intensity of SKS waves, measured by the amplitude of the transverse component, depends on the angle between the back azimuth of the earthquake and the direction of the symmetry axis and on the delay time δt between the two quasi-shear waves. It is shown that the splitting parameters can be determined from the azimuthal dependence of the splitting intensity, which is given by the first right eigenvector of the matrix containing the transverse components of all the records. Alternatively, the splitting intensity can be measured by projecting the transverse components on the radial components derivatives. Experiments on synthetic seismograms demonstrate that both approaches provide robust estimates of the splitting parameters. However, the projection approach gives measurements that are closer to the inputs and with smaller error bars, which suggests that it should be preferred when the signal-to-noise ratio is low. The new technique is applied to analyze shear wave splitting under stations BCAO (Bangui, Central African Republic) and BDFB (Brasilia, Brazil). The analysis of 75 seismograms recorded by station BCAO gives a fast polarization direction in very close agreement with the present-day motion direction of the African plate. Comparisons with the results of previous studies, obtained with other techniques and smaller data sets, suggest that some of the published measurements may be strongly biased. The main limitation of the multichannel analysis is a good azimuthal distribution of the seismicity. Maps of the azimuthal coverage were determined, and it is found that the most favorable regions to study anisotropy with SKS waves are a latitudinal band that goes from South America to Africa, the eastern part of North America, and India.

1. Introduction

Since strain-induced lattice-preferred orientation of highly anisotropic crystals such as olivine can produce anisotropy, seismic anisotropy studies can provide important constraints on the deformation of the upper mantle. As it enters an anisotropic region, a linearly polarized shear wave is split into two quasi-shear waves. The polarization of these waves is related to the properties of the anisotropic elasticity tensor. In the case of transverse isotropy with a horizontal axis of symmetry, two pulses will propagate: a fast pulse, polarized in the fast axis direction, and a slow pulse, polarized in the orthogonal direction. Upon propagation through the anisotropic layer, a delay time δt develops between the two pulses, whose magnitude depends both on the velocity difference between the fast and the slow directions and on the thickness of the layer.

Paper number 2000JB900199.
0148-0227/00/2000JB900199$09.00

The analysis of shear wave splitting is greatly simplified if the polarization of the incoming wave is known. In a pioneering study, *Vinnik et al.* [1984] used SKS waves, which are polarized in the radial direction, to study shear wave splitting under continental stations. Observations of shear wave splitting to constrain the anisotropy in the continental upper mantle have multiplied during the last decade. *Silver* [1996] presents an extensive review of the different results that were collected. Two different methods are commonly used to retrieve the fast shear wave polarization direction ϕ and the delay time δt. The first involves stacking the transverse components of many records coming from different directions with weights depending on azimuth [*Kosarev et al.*, 1984; *Vinnik et al.*, 1989b]. The direction ϕ is retrieved from the weights that give the maximum amplitude in the stack while δt is derived from this maximum amplitude of the stacked transverse components [*Vinnik et al.*, 1989b, 1998]. The second technique consists of finding the best inverse splitting operator, which minimizes the energy on the transverse component of a single record [*Silver and Chan*, 1988, 1991].

Both methods have advantages and shortcomings. The former relies on assumptions regarding the azimuthal dependence of the transverse component waveform. The validity of these assumptions is often difficult to assess objectively from the data. This method also lacks the possibility to constrain the measurement errors. The latter technique relies on the implicit assumption of transverse isotropy with an horizontal axis of symmetry, and thus provides apparent splitting parameters. Another limit is the signal-to-noise ratio (S/N) [*Restivo and Helffrich*, 1999], which can be somewhat compensated by a stacking technique similar, in principle, to the technique introduced by *Vinnik et al.* [1989a] [*Wolfe and Silver*, 1998]. Almost every published study uses either one of these techniques or some modified version of them. In this paper, I present a new multichannel technique, which robustly estimates the anisotropic parameters of the medium, even in the presence of strong noise in the records. I first describe the principles of the method and then show how it can be used to study shear wave splitting from SKS and $SKKS$ data.

2. Propagation of Shear Waves in Anisotropic Layers

Let us consider the simple case of an S wave propagating in a transversely isotropic medium, with a horizontal axis of symmetry. The model consists of a 30-km-thick anisotropic layer over an isotropic half-space. The parameters of the model are given in Table 1. Synthetic seismograms are computed for an incident plane SV wave for different azimuths. A ray parameter of 3.5 s/deg is used in the computation, which is a typical slowness for SKS. The modeling technique, described by *Kosarev et al.* [1979], utilizes the algorithm described by *Keith and Crampin* [1977a, b]. The synthetics are convolved with a pulse with a characteristic period of ~8 s, to reproduce the frequency content of SKS. The resulting traces for the radial and transverse components are shown in Figures 1a and 1b, respectively. The radial axis is in the horizontal plane and points toward the source. The transverse axis is obtained by a 90° clockwise rotation of the radial axis, looking from above. While the radial components do not show any significant variation with azimuth, the transverse component amplitudes show a 180° periodic dependence on azimuth. For the azimuths close to the directions of the fast and slow axis the signal on the transverse component disappear. Moreover, as a result of the splitting of the initially linearly polarized SV wave into two orthogonally polarized waves shifted in time, the transverse components look like the derivatives of the radial components (Figures 2a and 2b). These two important properties of shear wave splitting can be exploited to measure the parameters of anisotropy.

If $w(t)$ is the incoming wavelet and β the angle between the fast velocity axis and the radial axis, the signals on the radial and transverse components are given by [*Silver and Chan*, 1991]

$$R(t) = w(t+\delta t/2)\cos^2\beta + w(t-\delta t/2)\sin^2\beta \quad (1)$$

$$T(t) = -\frac{1}{2}[w(t+\delta t/2) - w(t-\delta t/2)]\sin 2\beta \quad (2)$$

For δt small compared to the dominant period of the signal, these expressions can be simplified as [*Silver and Chan*, 1988; *Vinnik et al.*, 1989b]

$$R(t) \approx w(t) \quad (3)$$

$$T(t) \approx -\frac{1}{2}(\delta t \sin 2\beta) w'(t)\ , \quad (4)$$

where $w'(t)$ is the time derivative of $w(t)$. Therefore the transverse component is simply the time derivative of the radial component multiplied by a sinusoidal factor whose amplitude depends on δt and whose phase depends on the fast axis orientation. In other words, the $M \times N$ matrix $\mathbf{T}$, generated from the transverse components of M records with N data points, can be written

$$\mathbf{T} = a\mathbf{s} \otimes \mathbf{r}\ , \quad (5)$$

where $a = -0.5$ is a constant factor, $\mathbf{s}$ is the splitting vector related to the amplitude variations of the transverse components with azimuth, and $\mathbf{r}$ is the radial component derivative. The circled cross represents the outer (or tensor) product between two vectors.

The right-hand side of (5) is identical to the first eigenimage of the matrix $\mathbf{T}$, given by $\lambda_1 \mathbf{u_1} \otimes \mathbf{v_1}$, where λ_1 is the first singular value of matrix $\mathbf{T}$, $\mathbf{u_1}$ is the first eigenvector of $\mathbf{T}\mathbf{T}^t$, and $\mathbf{v_1}$ is the first eigenvector of $\mathbf{T}^t\mathbf{T}$ [*Freire and Ulrych*, 1988]. This suggests that the singular value decomposition (SVD) of the data matrix $\mathbf{T}$ provides a natural and simple means to extract the splitting parameters.

For the set of synthetic seismograms without noise displayed in Figure 1, all the traces are equal within a scale factor that depends on azimuth. Therefore, $\mathbf{T}$ is of rank one and is fully described by the first eigenimage $\lambda_1 \mathbf{u_1} \otimes \mathbf{v_1}$. The splitting vector is defined by

Table 1. Model Parameters

Depth, km	ρ, g cm^{-3}	V_P, km s^{-1}	V_S, km s^{-1}	ϕ_0, deg	$\Delta V_S/V_S$	$\Delta V_S/V_S$	η
0-30	2.45	6.50	3.75	45	0.03	0.03	1.03
30-∞	3.40	8.15	4.70	-	-	-	-

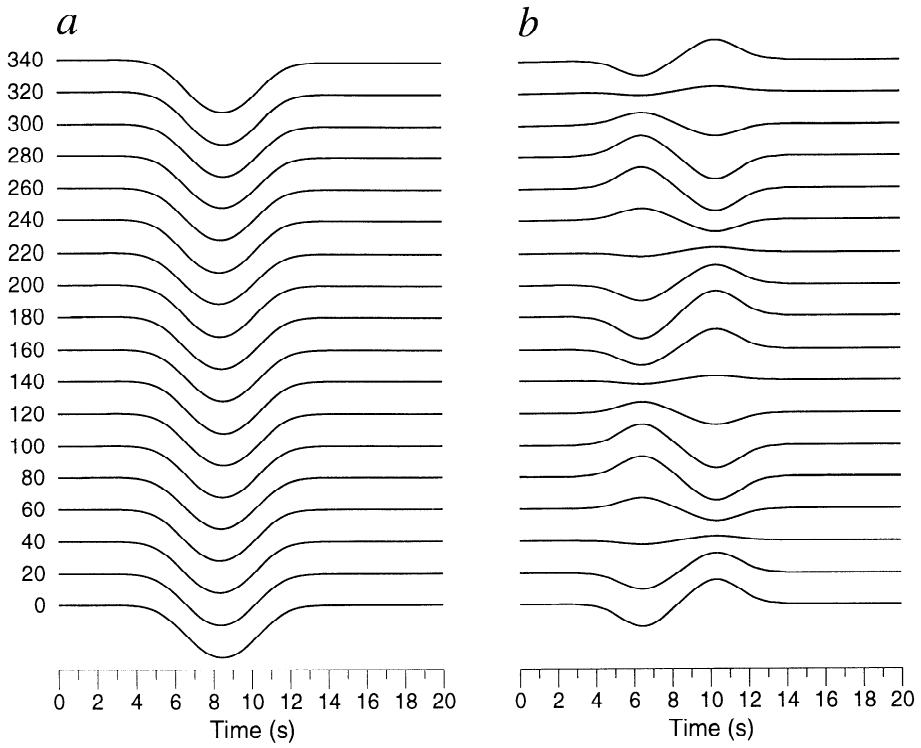

Figure 1. Synthetic seismograms computed in the model described in Table 1 for an incoming SV wave: (a) radial components and (b) transverse components. The numbers on the left indicate the azimuths.

$$\mathbf{s} = -2\frac{\lambda_1 \mathbf{u}_1}{||\mathbf{r}||}, \tag{6}$$

where $||\mathbf{r}||^2 = \mathbf{r}^t\mathbf{r}$ is the squared norm of $\mathbf{r}$. After normalization, the resulting splitting vector for a horizontal fast velocity axis should have the form $\delta t \sin[2(\phi - \phi_0)]$, with δt the delay time and ϕ_0 the azimuth of the fast axis. This is indeed observed in the splitting measurements which are plotted in Figure 3. In Figure 4, $\mathbf{v}_1$ is compared to the derivative of the radial component. The close similarity of the two waveforms demonstrates the efficiency of SVD for studying anisotropy. In the following, the azimuthal dependence of the splitting intensity will be referred to as the splitting function. For a horizontal axis of symmetry the splitting function is $\delta t \sin[2(\phi - \phi_0)]$. The splitting vector $\mathbf{s}$ is a sample of the splitting fuction at different azimuths obtained from a limited data set.

Alternatively, $\mathbf{s}$ can be determined directly by projecting the data on the radial component derivative $\mathbf{r}$, which is a better estimate of the waveform of the transverse component when S/N is low. In this case, the splitting vector is given by

$$\mathbf{s} = -2\frac{\mathbf{Tr}}{||\mathbf{r}||^2}. \tag{7}$$

It is possible to show that (7) gives the optimal estimate of the splitting vector (see Appendix A).

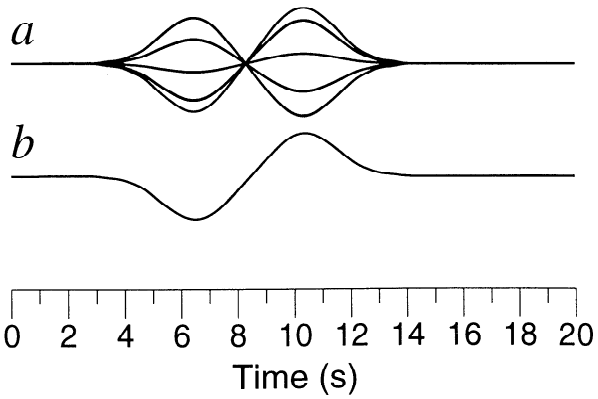

Figure 2. Same data as in Figure 1: (a) Synthetic transverse components and (b) derivative of the radial component.

3. Effects of a Dipping Axis of Symmetry

In order to investigate the effects of a dipping axis of symmetry, synthetic seismograms were computed in the model described in Table 1 but for three different dips of the fast axis: 30°, 45°, and 60°. In these modeling experiments the fifth elastic parameter F, or η, is needed to describe completely the elastic properties of the medium [*Babuška and Cara*, 1991]. The parameter η was fixed at 1.03, which is close to the value for an isotropic solid, for which $\eta = 1$. The corresponding splitting vectors $\mathbf{s}$ determined by SVD are shown in Fig-

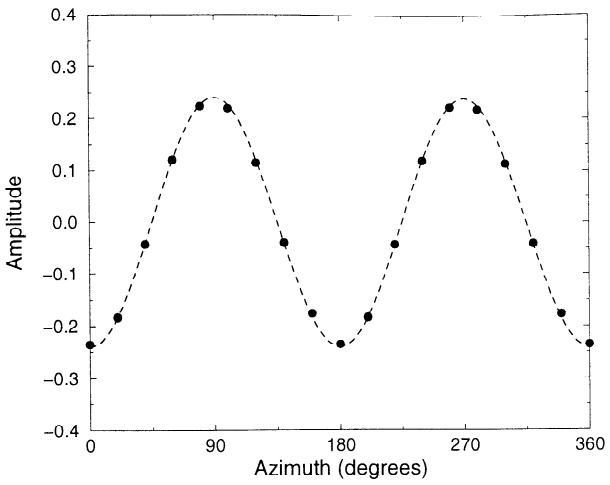

Figure 3. Splitting vector of the data shown in Figure 1b measured by SVD (solid circles) and the sinusoid determined by least squares fit (dashed line). The amplitude of the sinusoid is $\delta t = 0.24$ s, and its phase at the origin is $-2\phi_0 = -90°$.

ure 5. For dips smaller than 30° the splitting vector is undistinguishable from the splitting vector corresponding to the horizontal symmetry axis. For dips larger than 30° the symmetry break becomes apparent, generating a 360° periodic variation of the splitting vector. The extrema of the splitting function no longer have the same magnitude.

A simple way to estimate the relative contributions of the different azimuthal harmonics is provided by the discrete Fourier transform of the splitting vector:

$$S(k) = \sum_{j=1}^{N} s_j \exp\left(i\frac{2\pi k\phi_j}{360}\right) , \qquad (8)$$

where k is the azimuthal order, s_j and ϕ_j are the splitting amplitude and the back azimuth of the jth event, respectively, and N is the number of records. The amplitude of each azimuthal harmonic is then defined as

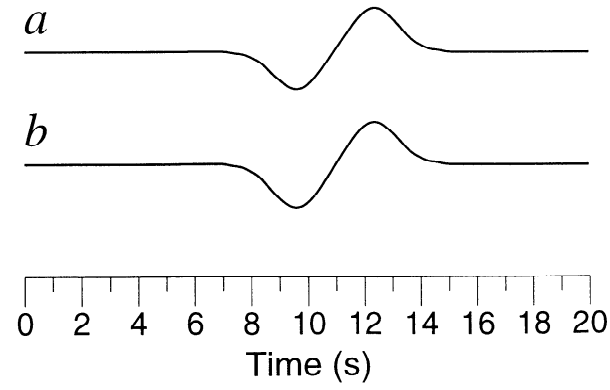

Figure 4. (a) Wavelet determined by SVD (right eigenvector $\mathbf{v_1}$) of the transverse components data shown in Figure 1b and (b) derivative of the radial component.

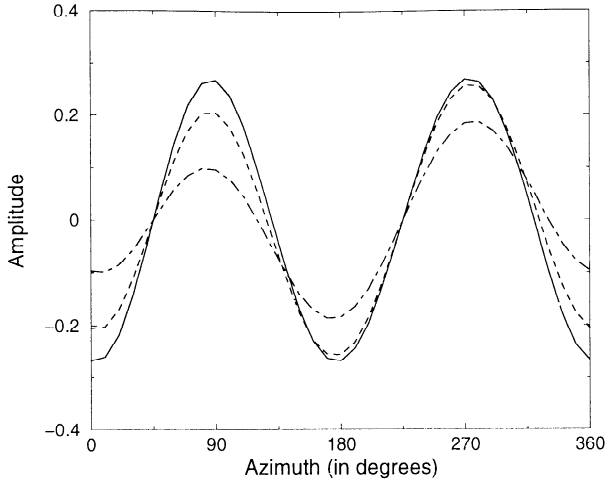

Figure 5. Splitting function as a function of azimuth for a fast axis dipping at 30° (solid line), 45° (dashed line) and 60° (dot-dashed line).

$$H(k) = \frac{2}{N}|S(k)| . \qquad (9)$$

The normalization is such that for a sinusoid with a period of $360/k$ degrees and a unit amplitude, $H(k) = 1$. Figure 6 shows the amplitude spectrum as a function of the azimuthal order k for two cases: a horizontal symmetry axis and a symmetry axis dipping at 60°. For the horizontal symmetry axis, the splitting function is monochromatic with a 180° period, and the amplitude spectrum has a single peak positionned at $k = 2$. When the fast axis is dipping, a 360° periodic variation of the splitting vector is introduced. As a result, the first azimuthal harmonic ($k = 1$) will have a nonzero amplitude. The amplitude and the phase of the first azimuthal harmonic depend on the parameter η, but a detailed investigation of this effect is beyond the scope of this paper. It is important to note that the splitting vector still gives valuable information even if the symmetry axis is not horizontal.

4. Measuring Shear Wave Splitting Parameters from the Splitting Vector s

4.1. The Measurement of ϕ and δt

When the splitting vector is determined, no assumptions are made regarding the anisotropic properties of the medium. It is only when we try to interpret the splitting vector in terms of anisotropy of the medium that some assumptions are made (sometimes implicitly). First, it is always assumed that the lateral variations of the anisotropy are small under the station and that the medium can be approximated by one (or sometimes two [see, e.g., *Savage and Silver*, 1993]) homogeneous anisotropic layer(s). Second, it is usually assumed that the axis of symmetry is horizontal. In this case, the second azimuthal harmonic is sufficient to constrain the anisotropy. In general, the information on the azimuth

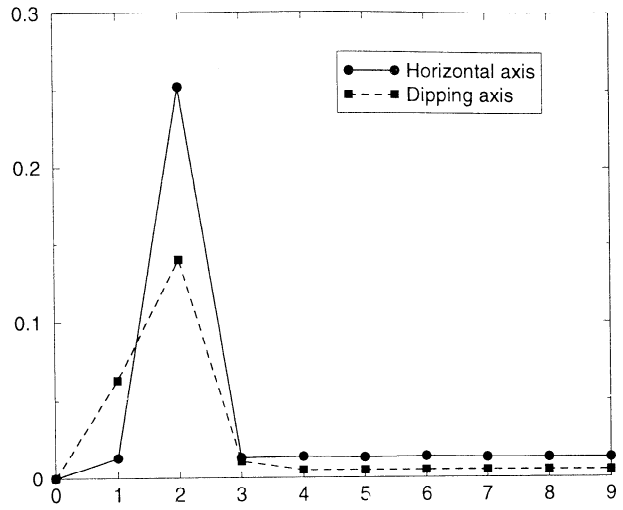

Figure 6. Amplitude of the azimuthal harmonics as a function of azimuthal order for a horizontal axis of symmetry (solid line) and for an axis dipping at 60° (dashed line).

and the dip of the symmetry axis is contained in the first two azimuthal harmonics. Higher-order harmonics, which will not be discussed here, are usually characterized by much smaller energies than the first two azimuthal harmonics. They describe the small deviations from the simple ideal model of a single anisotropic layer with no lateral variations of the anisotropic parameters. The ϕ and δt for the first two azimuthal harmonics can be determined from the normalized splitting vector by minimizing

$$\chi^2 = \sum_{i=1}^{M} \{p_i - [\delta t_1 \sin(\phi_i - \phi_1) + \delta t_2 \sin(2\phi_i - 2\phi_2)]\}^2 , \tag{10}$$

where M is the number of traces and p_i and ϕ_i are the splitting amplitude and azimuth of trace i, respectively. The δt_1 and δt_2 are the time shifts for the first and second azimuthal harmonics, respectively, while ϕ_1 and ϕ_2 are the phases of the first two azimuthal harmonics, which are related to the direction of the fast axis. The problem is equivalent to minimizing

$$\chi^2 = \sum_{i=1}^{M} [p_i - (x_1 \cos\phi_i + x_2 \sin\phi_i + x_3 \cos 2\phi_i + x_4 \sin 2\phi_i)]^2 , \tag{11}$$

where $\delta t_1 = \sqrt{x_1^2 + x_2^2}$, $\delta t_2 = \sqrt{x_3^2 + x_4^2}$, $\phi_1 = \tan^{-1}(-x_1/x_2)$ and $\phi_2 = 0.5 \tan^{-1}(-x_3/x_4)$. Let us define $X_1(\phi) = \cos\phi$, $X_2(\phi) = \sin\phi$, $X_3(\phi) = \cos 2\phi$, and $X_4(\phi) = \sin 2\phi$, and let $\mathbf{A}$ be a $M \times 4$ matrix whose components are defined by

$$A_{ij} = \frac{X_j(\phi_i)}{\sigma_i} , \tag{12}$$

with σ_i the uncertainty of each measured p_i (see Appendix B). If the vector $\mathbf{b}$ of length M is defined by

$$b_i = \frac{p_i}{\sigma_i} , \tag{13}$$

then minimizing (11) is equivalent to finding the vector $\mathbf{x}$ which minimizes

$$\chi^2 = |\mathbf{Ax} - \mathbf{b}|^2 . \tag{14}$$

This system is easily solved by using the SVD of the matrix $\mathbf{A} = \mathbf{U\Sigma V}$, where $\mathbf{U}$ is an $M \times M$ matrix whose columns $\mathbf{U_i}$ are the M eigenvectors of $\mathbf{AA}^t$, $\mathbf{V}$ is a 4×4 matrix whose columns $\mathbf{V_j}$ are the four eigenvectors of $\mathbf{A}^t\mathbf{A}$, and Σ is a $M \times 4$ diagonal matrix with λ_j the four singular values of $\mathbf{A}$ on its diagonal. The solution to the least squares problem (11) is then given by

$$\mathbf{x} = \sum_{k=1}^{4} \left(\frac{\mathbf{U_k b}}{\lambda_k} \right) \mathbf{V_k} . \tag{15}$$

The dashed line in Figure 3 represents the splitting function determined by this least squares minimization, which gives $\delta t_1 = 0$ s, $\delta t_2 = 0.24$ s, and $\phi_2 = 45°$. The anisotropic parameters are perfectly retrieved with this technique.

4.2. Measurement Errors

With the variances of the parameters x_j given by

$$\sigma_{x_j}^2 = \sum_{j=1}^{4} \left(\frac{V_{ij}}{\lambda_i} \right)^2 , \tag{16}$$

it is straightforward to compute the variance of the δt_i and ϕ_i:

$$\sigma_{\delta t_1}^2 = \sigma_{x_1}^2 \left(\frac{x_1}{\delta t_1} \right)^2 + \sigma_{x_2}^2 \left(\frac{x_2}{\delta t_1} \right)^2 \tag{17}$$

$$\sigma_{\delta t_2}^2 = \sigma_{x_3}^2 \left(\frac{x_3}{\delta t_2} \right)^2 + \sigma_{x_4}^2 \left(\frac{x_4}{\delta t_2} \right)^2 \tag{18}$$

$$\sigma_{\phi_1}^2 = \sigma_{x_2}^2 \left(\frac{x_2}{\delta t_1^2} \right)^2 + \sigma_{x_1}^2 \left(\frac{x_1}{\delta t_1^2} \right)^2 \tag{19}$$

$$\sigma_{\phi_2}^2 = \frac{1}{4} \left[\sigma_{x_4}^2 \left(\frac{x_4}{\delta t_2^2} \right)^2 + \sigma_{x_3}^2 \left(\frac{x_3}{\delta t_2^2} \right)^2 \right] \tag{20}$$

4.3. Resolution

The model resolution matrix $\mathbf{R}$ is given by [*Menke*, 1984]

$$\mathbf{R} = \mathbf{VV}^t . \tag{21}$$

In the synthetic case considered previously, the azimuthal coverage is homogeneous and the resolution matrix is the identity matrix, which means that the first two harmonics are perfectly resolved. In practice, the ability to resolve the first two azimuthal harmonics depends on the azimuthal distribution of the sources.

4.4. Noise Sensitivity

In the presence of noise the rank of **T** will be larger than 1. Eigenimages of rank larger than 1 will have significant energy and will mostly contain noise. However, the first eigenimage will still be dominated by the signal, and in most cases it should still be possible to separate the signal from the noise by conserving only the first eigenimage for further analysis.

For a validation of the multichannel technique and in order to investigate its robustness with respect to noise, different tests were performed on synthetic seismograms contaminated by noise. For a Gaussian random noise with variance σ_n^2, the eigenvectors of **T** are unchanged, but the singular values are given by $\lambda_{i,n}^2 = \lambda_i^2 + N\sigma_n^2$ [*Hemon and Mace*, 1978], where the λ_i are the singular values of **T** without noise. Therefore the splitting vector is still given by (6) using the first singular value corrected by the noise variance. In practice, Gaussian random noise is rarely met. To be close to natural observation conditions, the noise frequency content is estimated by averaging the power spectrum of different seismograms recorded by station BCAO (Bangui, Central African Republic) in time windows with no arrivals. The resulting power spectrum is used to generate random time series by randomization of the phase of the Fourier coefficients followed by inverse Fourier transform to the time domain. Then the noise sequences are multiplied by a constant factor and added to the synthetics to obtain a data set with a specified noise level. S/N is defined by the ratio between the maximum amplitude observed on all the transverse components and the noise root-mean-square (rms). Since the amplitude of the signal on the transverse component has sinusoidal variations with azimuth, the actual ratio between the signal amplitude and the noise rms will vary from one trace to another, and the definition gives a higher bound for this ratio.

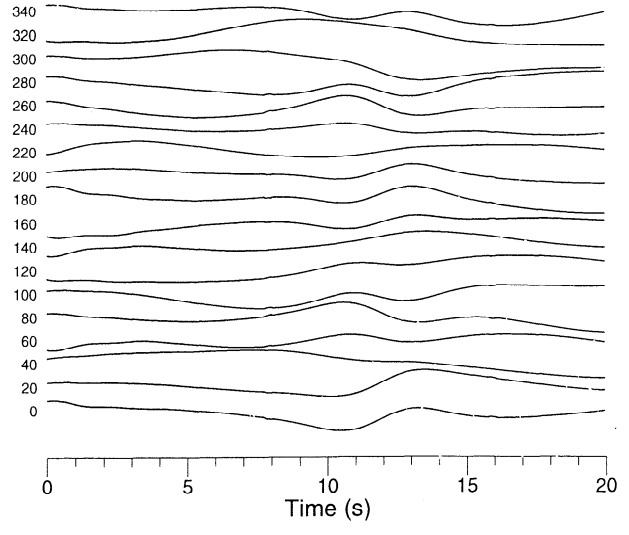

Figure 7. Synthetic seismograms with noise. The signal-to-noise ratio, defined as the ratio between the maximum amplitude observed on all the transverse components and the noise rms, is equal to 1.

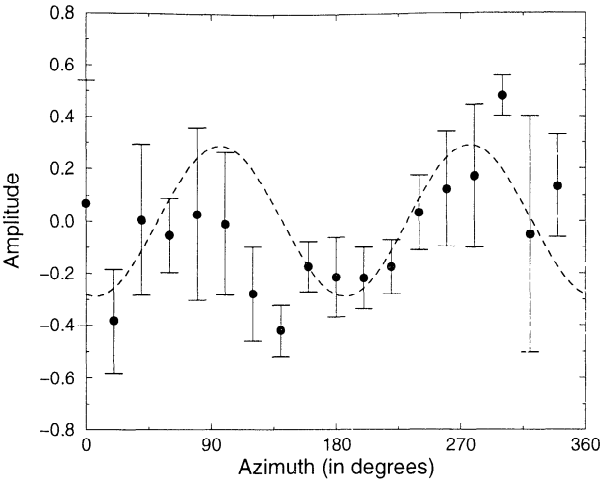

Figure 8. Splitting vector of the data shown in Figure 7 measured by SVD (solid circles) and the sinusoid determined by least squares fit (dashed line). The splitting parameters retrieved are $\phi_2 = 51 \pm 4°$ and $\delta t_2 = 0.29 \pm 0.06$ s.

Figure 7 shows the transverse component synthetics with S/N = 1, which is the limit for which it was possible to retrieve the input parameters within the error bars using the projection method. In figure 7, the signal appears strongly distorted, and it is clear that all the techniques based on the minimization of the energy on the transverse component [*Silver and Chan*, 1988; *Vinnik et al.*, 1989b] would give biased measurements.

The splitting vector determined by SVD is plotted in Figure 8. The least squares fit described in section 4 gives $\delta t_2 = 0.29 \pm 0.06$ s and $\phi_2 = 51 \pm 4°$. The individual splitting measurements (solid circles) show large deviations from the estimated splitting function (dashed line), and their uncertainties are quite large, but nevertheless, the splitting parameters are efficiently retrieved when all the data are considered simultaneously.

Figure 9 shows the splitting vector (solid circles), determined by projecting the data of Figure 7 on the radial components derivatives and the splitting function (dashed line), determined by analyzing the second azimuthal harmonic only. The measured parameters $\delta t_2 = 0.24 \pm 0.06$ s and $\phi_2 = 48 \pm 6°$ retrieve the input parameters within their error bars.

Both methods retrieve the direction of the fast axis and the delay time correctly. However, the projection method gives more accurate estimates of the splitting parameters. In this particular example, the first two singular values of **T** have similar magnitude. Therefore the separation of the signal from the noise by keeping the first eigenimage for the analysis is not perfect. To avoid any problem with SVD, a safe recommendation would be to examine systematically the singular values of **T** and to check that the first singular value is much larger than the others. In general, it may be appropriate

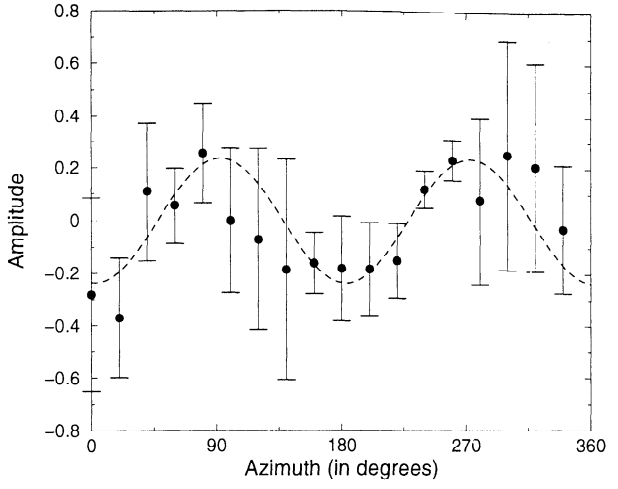

Figure 9. Splitting vector of the data shown in Figure 7 measured by projection on the radial component (solid circles) and the sinusoid determined by least squares fit (dashed line). The splitting parameters retrieved are $\phi_2 = 48 \pm 6°$ and $\delta t_2 = 0.24 \pm 0.06$ s.

to rely on the projection method rather than on the SVD in noisy environments.

5. Which Regions are Favorable for a Multichannel Analysis of Shear Wave Splitting?

A critical factor for the success of the multichannel analysis of shear wave splitting is the azimuthal coverage that can be obtained at a given location. Owing to the uneven distribution of earthquakes in the Earth, large spatial variations of the azimuthal coverage are expected. A direct assessment of the azimuthal coverage can be obtained by computing maps, following an approach similar to *Wysession* [1996]. For every location on the surface of the Earth the maps give the percentage of the azimuths covered by the seismicity that would be seen by a station installed at this particular point. The hypocenter catalog of *Engdahl et al.* [1998] has been scanned, and the events with a magnitude $m_b > 5.8$ and occurring after 1987 have been kept to generate a set of potentially favorable events. The magnitude threshold is a minimum requirement for an acceptable quality of the records. Keeping only recent events will also insure that high-quality broadband digital records are available. Thus the maps should give a fairly good representation of the potential interest of seismographic stations for shear wave splitting studies according to their location. Of course, data quality is another important parameter that should be incorporated during the evaluation procedure.

The azimuthal range is divided by 36 equal azimuthal windows of 10° width. The surface of the Earth is discretized with 5° × 5° cells. At the center of each cell the number of events in a given epicentral distance range that arrive in each of the 36 azimuthal windows is counted. The azimuthal coverage is defined as the number of azimuthal windows having at least one event and is thus an integer between 0 and 36. The two distance ranges 30°–90° and 90°–145° are investigated. The corresponding maps have been normalized by the maximum azimuthal coverage, 32 and 30, respectively. In the most favorable locations the whole azimuthal range is almost completely covered. However, these values drop to 19 and 16, respectively, if we measure the azimuthal coverage by only counting the azimuthal windows with more than 10 events. This means that relatively rare events contribute significantly to the azimuthal coverage. Therefore it would be appropriate to consider also the time period over which stations have been operational. The first map (Figure 10) gives an idea of the regions where P to S conversions at crustal discontinuities could be used to study crustal anisotropy. For this distance range a very good azimuthal sampling is expected for stations in eastern Asia, the northern Pacific, and Australia. A fair azimuthal sampling is also expected for stations in North America and western Europe. The second map (Figure 11) explores the SKS distance range. The best azimuthal coverages are found in a broad area that covers most of the Atlantic Ocean and Africa, as well as South America, in the eastern part of North America, and in India. The regions that are reasonably well covered in both distance ranges are the most favorable for studying the stratification of anisotropy, from the transition zone to the crust, by combining the information of both SKS and Ps phases. These regions are the eastern part of Australia, the northeastern part of America, and California, which are fortunately all well equipped with seismographic stations. Future efforts to constrain the distribution of anisotropy with depth, an important issue for a good interpretation of the splitting measurements, should focus on these regions.

For the sake of illustration, I present the application of the multichannel technique to SKS and $SKKS$ phases recorded at station BCAO (Bangui, Central African Republic; latitude 4.43°N, longitude 18.54°E) and BDFB (Brasilia, Brazil; latitude 15.64°S, longitude 48.01°W). Both stations offer a good azimuthal coverage for the distances of interest and have been operating for a long time.

6. Multichannel Analysis of SKS Splitting at Station BCAO

The data preprocessing objective is to produce records comparable to the data shown in Figure 1.

6.1. Data Preprocessing

Good quality records of SKS and $SKKS$ are first selected to cover the widest possible azimuthal range. These records are then low-pass filtered at 8 s and

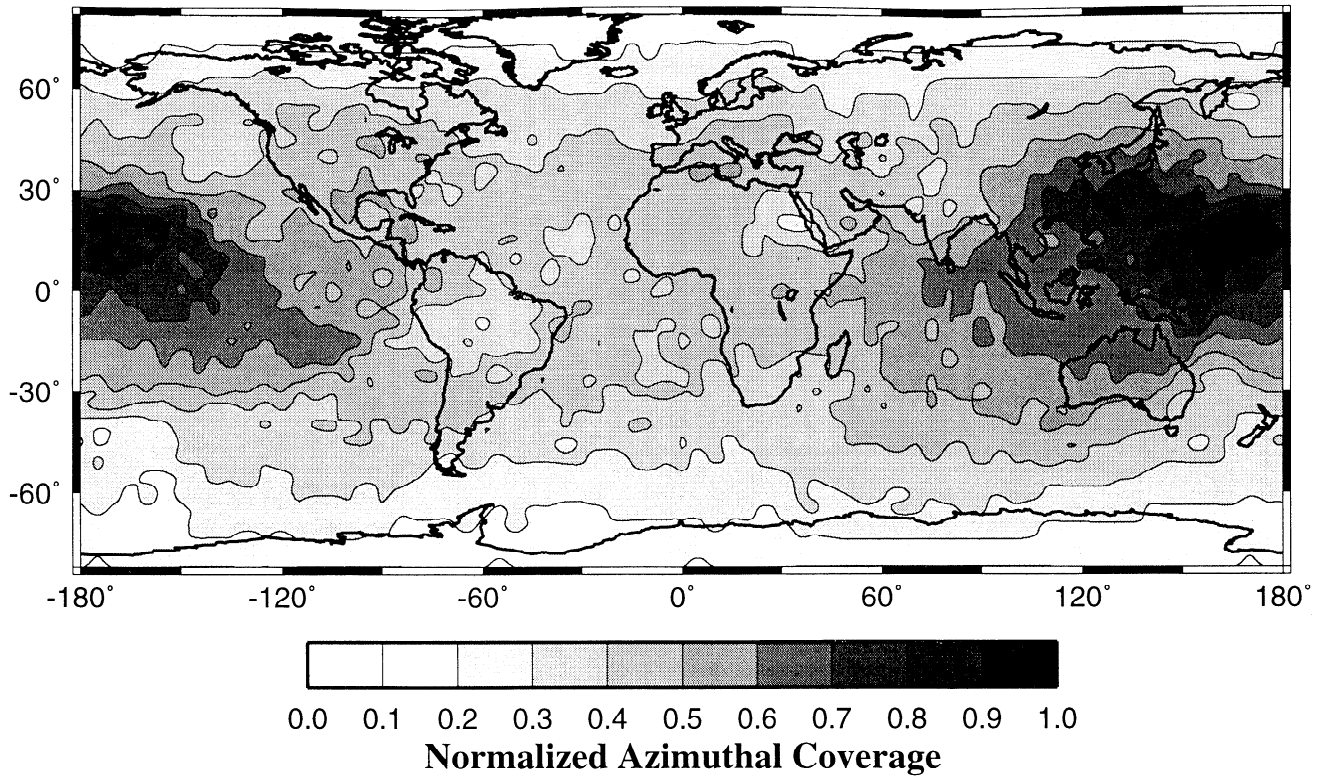

Figure 10. Map of the azimuthal coverage for the distance range 30°–90°. The values at each location represent the number of azimuthal windows covered by seismicity normalized to the maximum of the map.

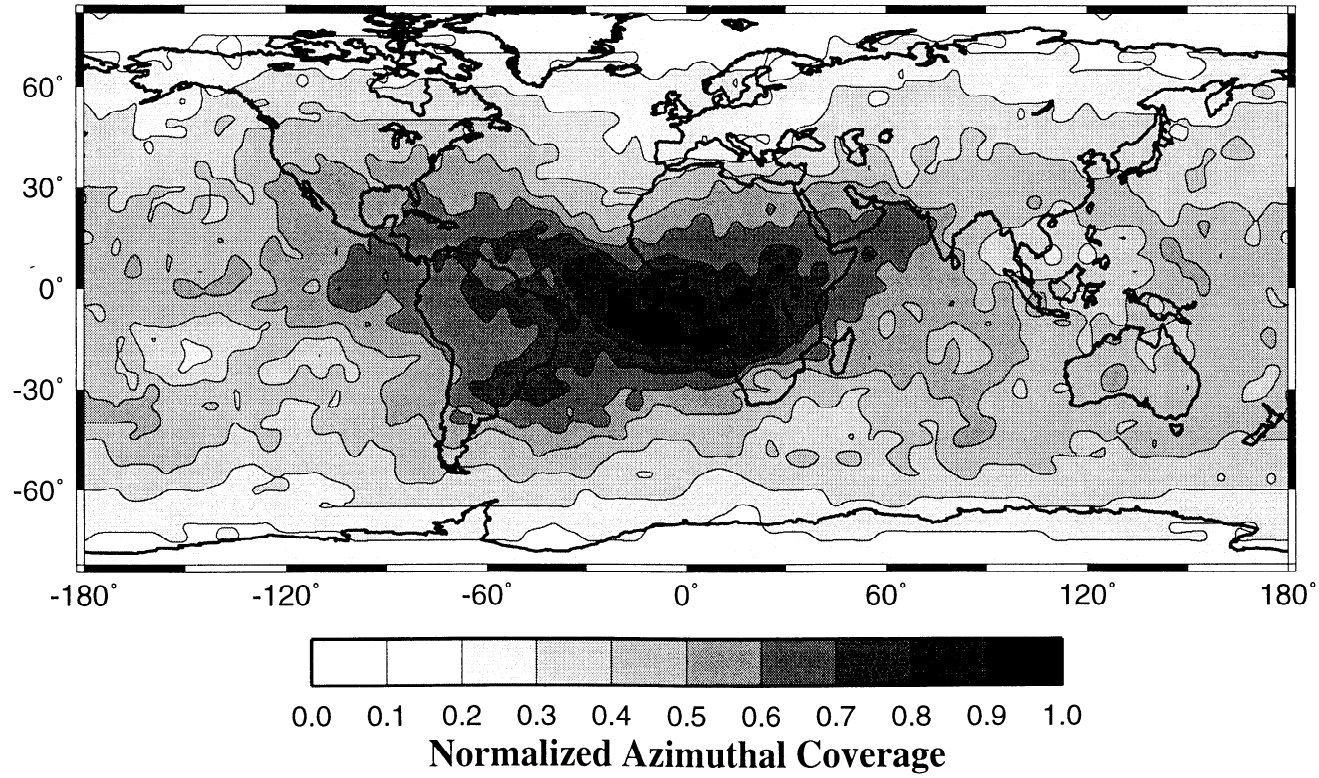

Figure 11. Same map as Figure 10, except for the distance range 90°–145°. The values at each location represent the number of azimuthal windows covered by seismicity normalized to the maximum of the map.

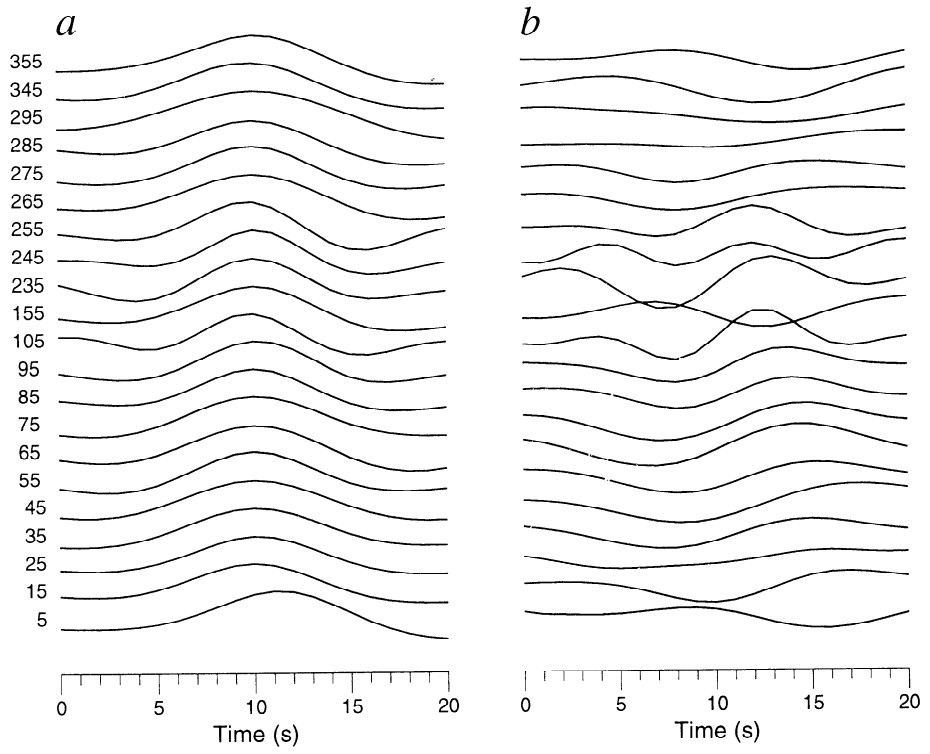

Figure 12. (a) SKS radial components recorded by station BCAO, after normalization and stack. (b) SKS transverse components, magnified by a factor 5. The numbers on the left indicate the azimuths.

standardized by deconvolving the radial and transverse components by the radial component. Finally, all the records are normalized so that the absolute magnitude on the radial components is unity. With real data, many factors such as scattering and attenuation can perturb the standardization, but the main challenge is the variation of the characteristic periods of SKS from one event to another. Since this variation has a significant effect on the amplitude of the transverse component, filtering the seismograms in the same frequency band is crucial. As a result of these steps, a set of 75 standardized traces corresponding to SKS or $SKKS$ phases was obtained. The data preprocessing is essentially the same as by *Vinnik et al.* [1998] but in this study, the data set is 3 times larger. To avoid biasing the results toward the azimuths with the most active seismicity, summary traces were computed by stacking the data found in different azimuthal windows. For this purpose, the width of the azimuthal windows was fixed at 10°. In this way, it is possible to get 21 azimuthal windows covered by the data, each window having an improved S/N in comparison to the one on the traces taken individually (Figure 12). Binning the data in azimuthal windows results in a loss of precision for the back azimuths, but for a random distribution of back azimuths this effect is negligible. Performing the analysis using different positions and/or smaller sizes of the azimuthal windows can improve the accuracy of the splitting measurements. For the cases discussed below, this is not necessary.

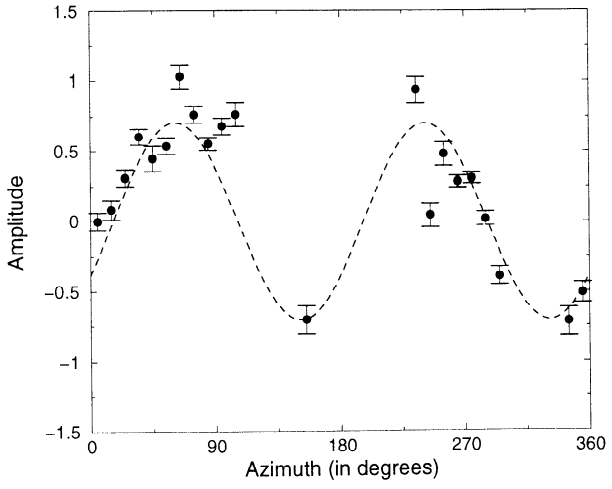

Figure 13. Splitting of the data shown in Figure 12b as a function of azimuth. The polarization curve determined by least squares fit is represented by the dashed line. The determined splitting parameters are $\phi_2 = 17 \pm 1°$ and $\delta t_2 = 0.74 \pm 0.03$ s.

6.2. Results

The splitting intensity as a function of back azimuth is measured by projecting each transverse component record on the derivative of the radial component, according to (7). The uncertainty of each splitting vec-

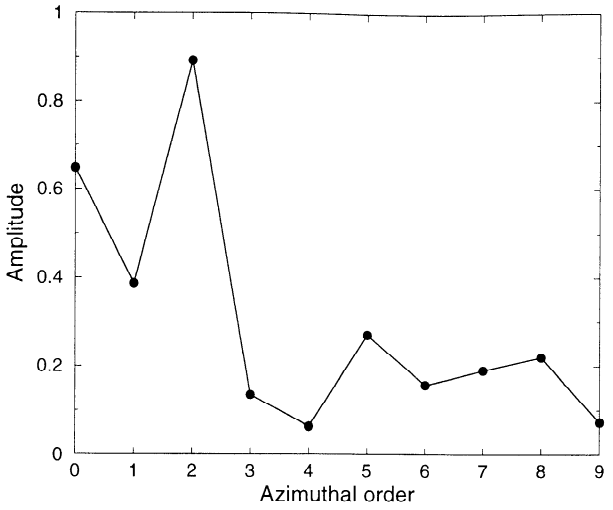

Figure 14. Amplitude of the azimuthal harmonics as a function of azimuthal order for station BCAO.

tor component is also determined following the method described in Appendix B. The results are displayed in Figure 13. There is very little seismicity to the south of station BCAO. However, the measurement at 135° is produced by analyzing a stack of three different events, which all consistently show large amplitudes with negative polarity. A striking 180° periodic azimuthal variation of the splitting vector is observed. This provides a direct evidence for the existence of an anisotropic layer with a subhorizontal axis of symmetry. The amplitude spectrum as a function of angular order is plotted in Figure 14. The second azimuthal harmonic dominates, but the spectrum shows significant amplitudes at almost every azimuthal order. This spectral leakage is a direct consequence of the limited and uneven distribution of back azimuths. Therefore, considering all the azimuthal orders, particularly the first one, in the least-squares fit is probably not justified, and only the second azimuthal harmonic will be analyzed. The fast axis direction $\phi_2 = 17 \pm 1°$ and delay time $\delta t_2 = 0.74 \pm 0.03$ s are found by minimizing (11). The anisotropic parameters determined by SVD, $\phi_2 = 16 \pm 1°$ and $\delta t_2 = 0.69 \pm 0.03$ s, are close to these measurements, which can be regarded as reliable. These azimuths are in remarkable agreement with the 23°E direction which can be inferred from the absolute rotation vector of the African plate given by *Minster and Jordan* [1978]. *Vinnik et al.* [1998] reported comparable values ($\phi_2 = 30 \pm 10°$ and $\delta t_2 = 0.6$ s) from a smaller data set and a different technique. However, these results differ significantly from a previous study where *Vinnik et al.* [1992] measured $\phi_2 = 60°$ and the same δt_2. This suggests that both the size of the data set and the technique can influence the measurements. The data quality for station BCAO can be rated as extremely good, and even larger discrepancies should be expected for stations with average or low quality.

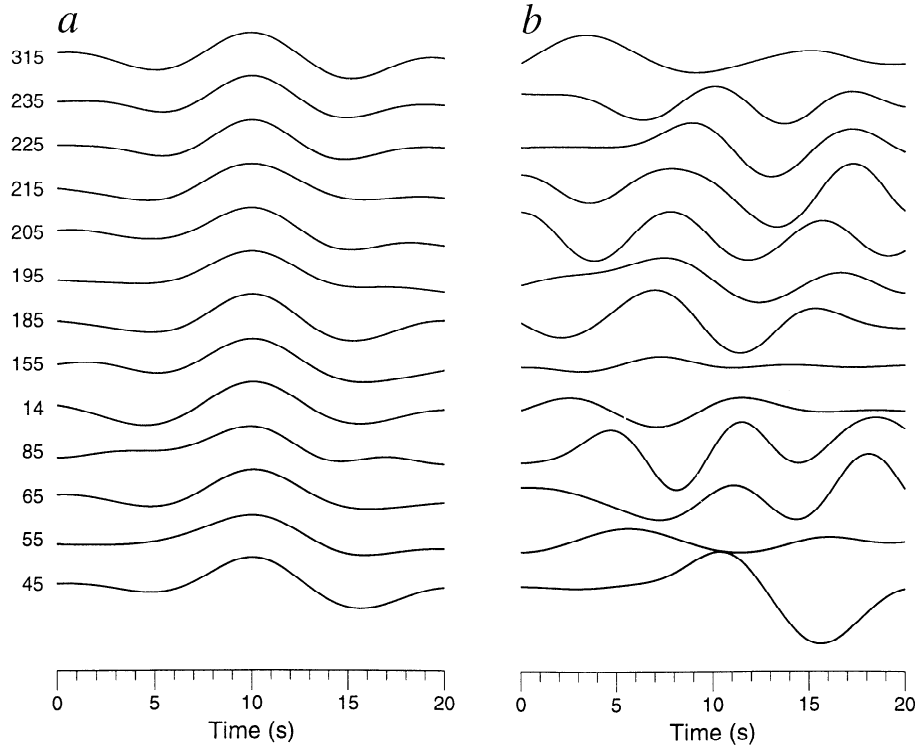

Figure 15. (a) *SKS* radial components recorded by station BDFB, after normalization and stack. (b) *SKS* transverse components, magnified by a factor 5. The numbers on the left indicate the azimuths.

7. Multichannel Analysis of SKS Splitting at Station BDFB

For station BDFB, 24 high-quality records of SKS are selected and binned into 10° wide azimuthal window to determine the splitting parameters (Figure 15). For this station, only 13 azimuthal windows are constrained by the data. The data processing is the same as for station BCAO. Figure 16 shows the splitting vector and the splitting function determined by least squares fit. Again, the 180° period is strongly expressed in the splitting vector. The splitting parameters determined from the analysis of the second azimuthal harmonic are $\phi_2 = 63 \pm 2°$ and $\delta t_2 = 0.94 \pm 0.06$ s, in agreement with *Russo and Silver* [1994], who reported $\phi_2 = 53°$ and $\delta t_2 = 1.5$ s.

8. Conclusions

The multichannel analysis of shear wave splitting is a natural and simple tool to constrain the splitting parameters. The tests on synthetic seismograms contaminated by strong noise demonstrate the robustness of this technique in cases where the classical techniques would fail. The ability to perform robust measurements with small and accurate error estimates in noisy environments or in regions where the anisotropy is weak is the main advantage of this technique. Additionally, all the available (good quality) data are used in the measurement process, in contrast to most of the previous studies that considered a very limited amount of data (typically less than five records and sometimes coming all from the same azimuthal window). The analysis of SKS and $SKKS$ recorded by station BCAO gives a fast velocity axis in close agreement with the absolute plate motion. Since this result strongly differs from a previous measurement, obtained with a different technique, this suggests that it may be necessary to reconsider some of the published results.

A promising aspect is the study of complex regions where stratification of anisotropy, usually diagnosed from an apparent variation of the splitting parameters with a 90° period, could be present. Different studies have reported such a periodic variation of the splitting parameters with azimuth [*Savage and Silver*, 1993; *Wolfe and Silver*, 1998; *Levin et al.*, 1999]. An important aspect of these studies is that they need apparent splitting parameters measurements for a broad range of azimuths. The azimuths close to either the apparent fast or slow axis for which the energy on the transverse component is small are poorly constrained by classical techniques. The multichannel technique should be appropriate to analyze shear wave splitting in this context.

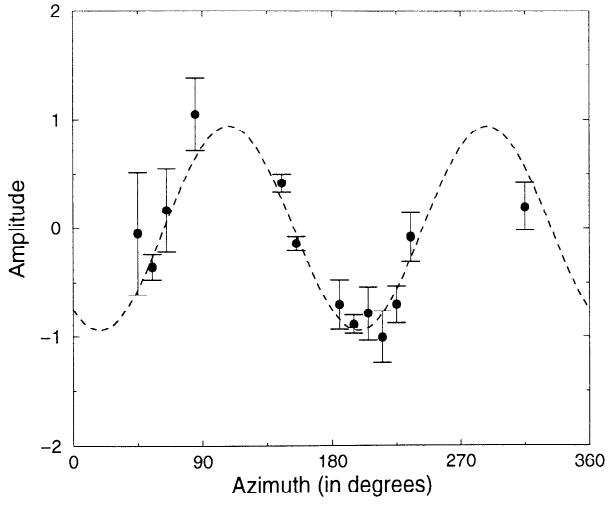

Figure 16. Splitting of the data shown in Figure 15b, as a function of azimuth. The polarization curve determined by least squares fit is represented by the dashed line. The determined splitting parameters are $\phi_2 = 63 \pm 2°$ and $\delta t_2 = 0.94 \pm 0.06$ s.

Appendix A: The Multichannel Analysis as an Optimal Estimator of the Splitting Vector

The $M \times N$ matrix $\mathbf{T}$ which contains the M deconvolved transverse component records with N data points has the form

$$\mathbf{T} = -\frac{1}{2}\mathbf{s} \otimes \mathbf{r} + \mathbf{N}\,, \tag{A1}$$

where $\mathbf{r}$ is the radial component derivative, $\mathbf{s}$ is the splitting vector, and $\mathbf{N}$ is the noise matrix. The mean-square error for the ith trace (channel) is

$$E_i = \frac{1}{N}\sum_{j=1}^{N}\left(T_{ij} + \frac{1}{2}s_i r_j\right)^2 . \tag{A2}$$

We want to find the ith component of the splitting vector that minimizes the error E_i. Therefore s_i is given by

$$\frac{\partial E_i}{\partial s_i} = \frac{1}{N}\sum_{j=1}^{N}\left(\frac{1}{2}s_i r_j^2 + r_j T_{ij}\right) = 0\,. \tag{A3}$$

After simplification, one obtains

$$s_i = -\frac{\sum_{j=1}^{N} 2T_{ij}r_j}{\|\mathbf{r}\|^2}\,, \tag{A4}$$

which is similar to (7).

Appendix B: Uncertainty of the Splitting Vector Estimates

Using (A1) and (A4), the variance of s_i writes

$$\sigma_i^2 = \frac{1}{N\|\mathbf{r}\|^2}\left(-\frac{1}{2}s_i\mathbf{r} - \frac{\mathbf{r}^t\mathbf{T_i}}{\mathbf{r^t r}}\mathbf{r}\right)^2\,, \tag{B1}$$

where $\mathbf{T_i}$ is the ith row of $\mathbf{T}$. From (B1) it is straightforward to show that $\sigma_i^2 = E_i$. Therefore using (A2) the error associated to each s_i is given by

$$\sigma_i = \sqrt{\frac{1}{N}\sum_{j=1}^{N}\left(T_{ij} + \frac{1}{2}s_i r_j\right)^2}, \qquad \text{(B2)}$$

and after simplification

$$\sigma_i = \sqrt{\frac{1}{N}\left(\sum_{j=1}^{N} T_{ij}^2 - \frac{1}{4}\|\mathbf{r}\|^2 s_i^2\right)}. \qquad \text{(B3)}$$

If the splitting vector is determined with SVD, σ_i is then given by:

$$\sigma_i = \sqrt{\frac{1}{N}\sum_{j=1}^{N}\left(T_{ij} - \lambda_1 u_i v_j\right)^2}, \qquad \text{(B4)}$$

where λ_1 is the first singular value of $\mathbf{T}$, u_i is the ith component of the first right eigenvector $\mathbf{u_1}$ and v_j is the jth component of the first left eigenvector $\mathbf{v_1}$.

Acknowledgments. This research was supported by the David and Lucile Packard Fondation awarded to R. van der Hilst and a Lavoisier fellowship. I would like to thank K. Fischer, S. Kaneshima, and the Associate Editor G. Helffrich for their careful and thoughtful review of the manuscript. This work benefitted from stimulating discussions with L. Vinnik, G. Kosarev, V. Levin, J. Park, W. Menke, and R. van der Hilst.

References

Babuška, V., and M. Cara, *Seismic anisotropy of the Earth*, Kluwer Acad., Norwell, Mass., 1991.

Engdahl, E. R., R. D. van der Hilst, and R. P. Bulland, Global teleseismic earthquake relocation with improved travel times and procedures for depth determination, *Bull. Seismol. Soc. Am.*, *88*, 722–743, 1998.

Freire, S. L. M., and T. J. Ulrych, Application of singular value decomposition to vertical seismic profiling, *Geophysics*, *53*, 778–785, 1988.

Hemon, C., and D. Mace, Essai d'une application de la transformation de Karhunen-Loève au traitement sismique, *Geophys. Prospect.*, *26*, 600–626, 1978.

Keith, C. M., and S. Crampin, Seismic body waves in anisotropic media: Reflections and refraction at an interface, *Geophys. J. R. Astron. Soc.*, *49*, 181–208, 1977a.

Keith, C. M., and S. Crampin, Seismic body waves in anisotropic media: Propagation through a layer, *Geophys. J. R. Astron. Soc.*, *49*, 209–223, 1977b.

Kosarev, G. L., L. I. Makeyeva, E. F. Savarensky, and E. M. Chesnokov, Influence of anisotropy beneath seismograph station on body waves, *Izv. Acad. Nauk. Fiz. Zemli*, *2*, 26–37, 1979.

Kosarev, G. L., L. I. Makeyeva, and L. Vinnik, Anisotropy of the mantle inferred from observations of P to S converted waves, *Geophys. J. R. Astron. Soc.*, *76*, 209–220, 1984.

Levin, V., W. Menke, and J. Park, Shear-wave splitting in the Appalachians and the Urals: A case for multilayered anisotropy, *J. Geophys. Res.*, *104*, 17,975–17,993, 1999.

Menke, W., *Geophysical Data Analysis: Discrete Inverse Theory*, Academic Press, San Diego, Calif., 1984.

Minster, J. B., and T. H. Jordan, Present-day plate motions, *J. Geophys. Res.*, *83*, 5331–5354, 1978.

Restivo, A., and G. Helffrich, Teleseismic shear wave splitting measurements in noisy environments, *Geophys. J. Int.*, *137*, 821–830, 1999.

Russo, R. M., and P. G. Silver, Trench-parallel flow beneath the Nazca plate from seismic anisotropy, *Science*, *263*, 1105–1111, 1994.

Savage, M. K., and P. G. Silver, Mantle deformation and tectonics: Constraints from seismic anisotropy in the western United States, *Phys. Earth Planet. Inter.*, *78*, 207–227, 1993.

Silver, P. G., Seismic anisotropy beneath the continents: Probing the depths of geology, *Annu. Rev. Earth Planet. Sci.*, *24*, 385–432, 1996.

Silver, P. G., and W. W. Chan, Implications for continental structure and evolution from seismic anisotropy, *Nature*, *335*, 34 39, 1988.

Silver, P. G., and W. W. Chan, Shear wave splitting and subcontinental mantle deformation, *J. Geophys. Res.*, *96*, 16,429–16,454, 1991.

Vinnik, L., G. L. Kosarev, and L. I. Makeyeva, Anisotropy of the lithosphere from the observations of *SKS* and *SKKS*, *Proc. Acad. Sci. USSR*, *278*, 1335–1339, 1984.

Vinnik, L., V. Farra, and B. Romanowicz, Azimuthal anisotropy in the Earth from observations of *SKS* at GEOSCOPE and NARS broadband stations, *Bull. Seismol. Soc. Am.*, *79*, 1542–1558, 1989a.

Vinnik, L., R. Kind, G. L. Kosarev, and L. I. Makeyeva, Azimuthal anisotropy in the lithosphere from observations of long-period S-waves, *Geophys. J. Int.*, *99*, 549–559, 1989b.

Vinnik, L., L. I. Makeyeva, A. Milev, and Y. Usenko, Global patterns of azimuthal anisotropy and deformations in the continental mantle, *Geophys. J. Int.*, *111*, 433–447, 1992.

Vinnik, L., S. Chevrot, and J. P. Montagner, Seismic evidence of flow at the base of the upper mantle, *Geophys. Res. Lett.*, *25*, 1995–1998, 1998.

Wolfe, C. J., and P. G. Silver, Seismic anisotropy of oceanic upper mantle: Shear wave splitting methodologies and observations, *J. Geophys. Res.*, *103*, 749–771, 1998.

Wysession, M. E., How well do we utilize global seismicity?, *Bull. Seismol. Soc. Am.*, *86*, 1207–1219, 1996.

S. Chevrot, Department of Earth, Atmospheric and Planetary Sciences, Massachusetts Institute of Technology, Cambridge, MA 02139. (chevrot@quake.mit.edu)

(Received November 1, 1999; revised May 9, 2000; accepted June 1, 2000.)